Facile synthesis and characterization of WO_3–Al_2O_3 nanocomposites as an effective photocatalyst for degradation of Congo red under UV and visible light irradiation

Mahzad Firouzi, Azita Nouri*

*Department of Chemistry, Shahr-e-Qods Branch, Islamic Azad University, Tehran, Iran, Tel. +98(912)2005284;
emails: nouria244@gmail.com (A. Nouri), mahzadfiroozi@gmail.com (M. Firouzi)*

ABSTRACT

For the purpose of this study, sol-gel method at different molar ratios was used to prepare WO_3–Al_2O_3 nanocomposites. Then, the synthesized nanocomposites were characterized by different techniques including Fourier transform infrared spectroscopy, field emission scanning electron microscopy coupled with energy-dispersive spectroscopy, X-ray diffraction, photoluminescence spectroscopy, adsorption–desorption N_2 isotherms Brunauer–Emmet–Teller and Barrett–Joyner–Halenda. The results revealed that the specific surface area of WO_3 nanoparticles (NPs) increased from 2.83 to 41.80 m^2 g^{-1} due to the incorporation of Al_2O_3 in the composite. Moreover, the photocatalytic activity of the samples was evaluated in the degradation of Congo red (CR) in aqueous solution under UV and visible light irradiation with optimization of different parameters. The photocatalytic activity of the WO_3–Al_2O_3 nanocomposites was compared with pure WO_3 NPs and photocatalytic performance of the WO_3 NPs increased by incorporation of Al_2O_3 in the composite. Finally, the degradation percentage of CR was *achieved* 100% within 30 min by changing molar ratio, pH and catalyst dosage. The enhanced photocatalytic performance was attributed to the increased specific surface area and decreased electron–hole pair recombination.

Keywords: WO_3–Al_2O_3 nanocomposites; Sol-gel; Photocatalytic degradation; Congo red

1. Introduction

Nowadays, large amount of hazardous organic pollutants containing textile industry, pharmaceutics, sanitary and discharged into the environment [1,2] are attached to the industrial activities resulting in a serious global environmental issue [3]. One of the synthetic dyes in textile is Congo red (CR), which is an anionic dye used in leather, and paper and pulp industries [4]. As CR has azo (−N=N−) groups and stable aromatic ring [5–7], it can cause cancer and burning effects on eyes, nausea and skin diseases [8,9]. Therefore, several methods have been suggested for the elimination of this compound from wastewater in the literature, which can be mentioned to advanced oxidation processes method for the destruction of organic and biological pollutants [10]. These processes of semiconductors are used as photocatalyst with both, an UV or visible irradiation for decomposition of organic molecules [11,12]. WO_3 nanoparticles (NPs) are known as a good photocatalyst and one of the *n*-type semiconductors as well, which has a band gap 2.80 eV [13–15]. WO_3 NPs has been used for photocatalytic degradation of organic pollutants in wastewater. The photocatalytic performance of WO_3 NPs is hindered by fast recombination rate of the photo-generated electron–hole pairs [16]. In order to enhance the photocatalytic performances of WO_3 NPs, various methods such as choosing appropriate synthesis method, preparing composite photocatalyst and semiconductor oxides doped with metal ions has been applied [17–19]. Therefore, a large number of photocatalysts have been used for degradation of CR such as grapheme/polyaniline/cuprous oxide composite

* Corresponding author.

[20], Pd-doped ZnO [21], WO_3 NPs [22], SnO_2 NPs [23], W-S-N-tri doped TiO_2 [24], $Pd-Bi_{3.84}W_{0.16}O_{6.24}$ nanocomposite [25], and TiO_2 NPs [26] but there has not been any research about the use of $WO_3–Al_2O_3$ nanocomposite as photocatalyst for degradation of CR. This study was performed using Al_2O_3 as a support for WO_3 NPs due to its benefits including high surface area and decreased electron–hole pair recombination. $WO_3–Al_2O_3$ nanocomposites were synthesized by a simple sol-gel method at different molar ratios of $WO_3–Al_2O_3$. The prepared photocatalysts were characterized by X-ray diffraction (XRD), Fourier transform infrared spectroscopy (FTIR), field emission scanning electron microscopy (FESEM), energy-dispersive spectroscopy (EDS), photoluminescence (PL) spectroscopy, Brunauer–Emmet–Teller (BET) and Barrett–Joyner–Halenda (BJH) and the photocatalytic performances were compared for degradation of CR under UV and visible light irradiation. This study was an attempt to investigate the effects of various operating parameters, for instance, molar ratio, pH, and catalyst dosage on degradation of CR.

2. Experimental Setup

2.1. Materials

All the chemicals used in this study, including tungstate dehydrate ($Na_2WO_4·2H_2O$), thiourea (CH_4N_2S), nitric acid (HNO_3), aluminum nitrate nonahydrate [$Al(NO_3)_3·9H_2O$], ammonia solution (NH_4OH), tetramethylammonium hydroxide (Me_4NOH), sodium hydroxide (NaOH), and hydrochloric acid (HCl) were purchased from Merck chemicals. The CR dye from Merck Company (Germany) is used as a model organic pollutant in this study. Double-distilled water was used throughout the experiments unless otherwise stated. The physical and chemical properties of the CR used in this study are summarized in Table 1.

2.2. Preparation of photocatalysts

2.2.1. Synthesis of WO_3 NPs

WO_3 NPs were prepared by precipitation method. First, amounts of sodium tungstate dehydrate (0.05 mol L^{-1}) were dissolved in double-distilled water and added into amounts

of a nitric acid solution (10% v/v, HNO_3) under stirring at 80°C. Then 70 mL of thiourea (0.0064 mol L^{-1}) was added to the solution under continuous stirring. The formed yellow-green solid precipitated, then dried at 150°C for 2 h in an oven and finally calcined at 500°C for 2 h in a muffle furnace to obtain WO_3 NPs [27].

2.2.2. Synthesis of Al_2O_3 NPs

Al_2O_3 NPs were synthesized by a simple wet chemical method. In total, 200 mL of aluminum nitrate nonahydrate solution (0.1 mol L^{-1}) was stirred on a magnetic stirrer and heated to 60°C. Then ammonia solution (2 mol L^{-1}) was added dropwise to the solution, while continuously stirring the solution at a constant pH and temperature (60°C) for 1 h. The formed aluminum hydroxide gel is allowed to cool down to room temperature for 1 h and then washed several times with double-distilled water and then it was dried in hot air oven at 150°C for 6 h. Finally, it was heated at a final temperature 550°C for 4 h in a muffle furnace [28].

2.2.3. Synthesis $WO_3–Al_2O_3$ nanocomposites

The $WO_3–Al_2O_3$ nanocomposites were synthesized by sol-gel method, which is the simple and low temperature and pressure method for the synthesis of nanostructured metal oxides. Three different molar ratios of $WO_3–Al_2O_3$ (1:1, 1:2, 2:1) were used in this study. First, amounts of WO_3 nanopowder was taken in a beaker at room temperature under air atmosphere. This solution was added to 50 mL of double-distilled water under stirring for 30 min, and added to the amounts of aluminum hydroxide gel, while continuously stirring the solution. This mixture was sonicated for 30 min at room temperature and then 7.5 mL of tetramethylammonium hydroxide (TMAH) solution (0.28 mol L^{-1}) was added and stirred vigorously for 30 min. At the end of this step, 7.5 mL of TMAH (0.28 mol L^{-1}) was added. The obtained precipitate was dried in hot air oven at 100°C and then calcined at 600°C for 3 h in a muffle furnace. The designation of different $WO_3–Al_2O_3$ nanocomposites prepared under different synthetic conditions is given in Table 2.

2.3. Characterization

The crystal structure of the synthesized samples was identified by XRD technique (Model X-pert pro, PANalytical, Netherlands). The CuK_α radiation ($\lambda = 1.5406$ Å) was operated at 40 kV and 40 mA in the 2θ range of 10°–80°. The surface morphology of the
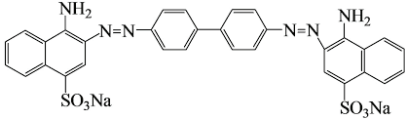
Table 1
Summary of Congo red

Characteristic	Congo red
Molecular structure	
Molecular formula	$C_{32}H_{22}N_6Na_2O_6S_2$
Molecular weight	696.663219 g mol^{-1}
Dye class	Azo
pK_a	4.1:3.0
Melting point	360°C
pH range	3.0–5.0
Density	0.995 g cm^{-3} at 25°C

Table 2
Nomenclature of different nanocomposites prepared in the present study

$WO_3–Al_2O_3$ ratio	Amount of $Na_2WO_4·2H_2O$ (M)	Amount of $Al(NO_3)_3·9H_2O$ (M)
1:1	0.1	0.1
1:2	0.1	0.2
2:1	0.2	0.1

samples were characterized using a FESEM (Model Zeiss, Sigma, Germany) operated at 15 kV coupled with an energy-dispersive spectrometer (EDS). FTIR (Model Vertex 80, Bruker, Germany) was used for recording IR spectra in the range of 4,000–400 cm^{-1} using the KBr pellet method. Specific surface area and pore volume of the photocatalysts were measured by nitrogen adsorption isotherms and using a NOVA 2000 (Quantachrome, USA) instrument by means of the BET equation, the samples were perfectly degassed at 300°C for 5 h. Furthermore, PL spectra of photocatalysts were obtained with an Avant spectrophotometer (Avaspec-2048-TEC). At the end, photocatalytic degradation of CR was studied using a UV–visible spectrophotometer (Model UV-1800, Shimadzu, Japan) at a working wavelength range of 200-800 nm.

2.4. Evaluation of photocatalytic activity

The photocatalytic activities of the prepared WO$_3$ NPs and WO$_3$–Al$_2$O$_3$ nanocomposites were evaluated by employing CR as the model pollutant in aqueous solution using a photocatalytic reactor under UV and visible light irradiation. A 30 W UV-C light and 100 W Tungsten lamp were used as the source of UV light and visible light, respectively. In each experiment, 0.1 g of photocatalyst was dispersed in 100 mL of CR solution (5 mg L^{-1}). Before UV-light irradiation at room temperature, the suspension was magnetically stirred in the dark for 15 min to the establishment of an ensured adsorption/desorption equilibrium between photocatalyst and Congo red. At a given irradiation time intervals, about 15 mL of the solution were withdrawn and centrifuged to separate the catalyst particles. Then, the characteristic absorption peak at 498 nm of CR was used for monitoring the photocatalytic degradation process by an UV–Vis spectrophotometer. The degradation efficiencies of CR were calculated as follows:

$$\text{Degradation (\%)} = \frac{A - A_0}{A_0} \times 100 \tag{1}$$

where A_0 represents the initial absorbance, and A is the change in absorbance of the CR at the absorption characteristics wavelength of 498 nm.

3. Results and discussion

3.1. FTIR analysis

FTIR spectra of WO$_3$ NPs, Al$_2$O$_3$ NPs [29] and WO$_3$–Al$_2$O$_3$ nanocomposites are shown in Fig. 1. The O–W–O stretching vibration of WO$_3$ crystals are observed at 820 cm^{-1} (Fig. 1(a)) [30]. The peaks in the range 3,250–3,690 cm^{-1} associated with the –OH stretching band (Figs. 1(b)–(e)) [31]. The H–O–H scissor mode is located about 1,620 cm^{-1} (Fig. 1(b)) which is associated with water species [32,33]. Therefore, the absorption band at 1,630 cm^{-1} is attributed to the H–O–H scissoring mode. The absorption peaks at 884.39 and 554.18 cm^{-1} are related to the Al–O stretching vibration and O–Al–O bending vibration, respectively [34]. The IR bands of WO$_3$–Al$_2$O$_3$ nanocomposites around 880 and 637 cm^{-1} are observed that are attributed to O–W–O stretching vibration and O–Al–O bending vibration, respectively.
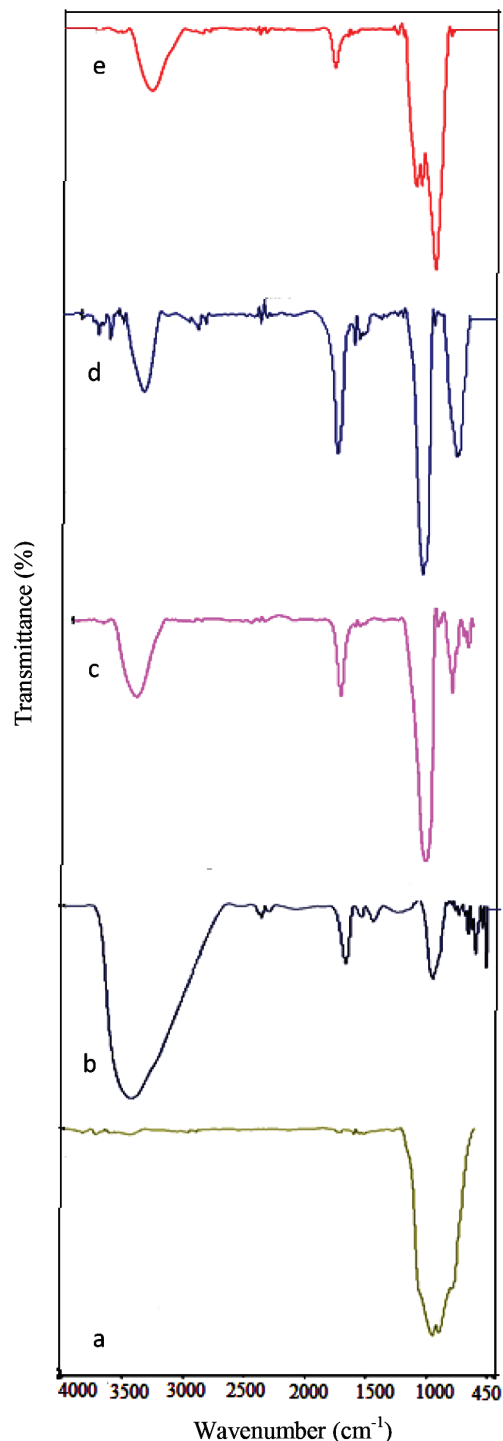

Fig. 1. FTIR spectra of (a) WO$_3$ NPs, (b) Al$_2$O$_3$ NPs [29] and WO$_3$–Al$_2$O$_3$ nanocomposites with different molar ratios: (c) (1:1), (d) (1:2) and (e) (2:1).

3.2. FESEM and EDS analysis

The FESEM images of WO$_3$ NPs, Al$_2$O$_3$ NPs [29] and WO$_3$–Al$_2$O$_3$ nanocomposites are shown in Fig. 2. Fig. 2(a) illustrates that WO$_3$ NPs are uniform particles size and spherical shapes with some agglomeration [35]. In Fig. 2(b) small
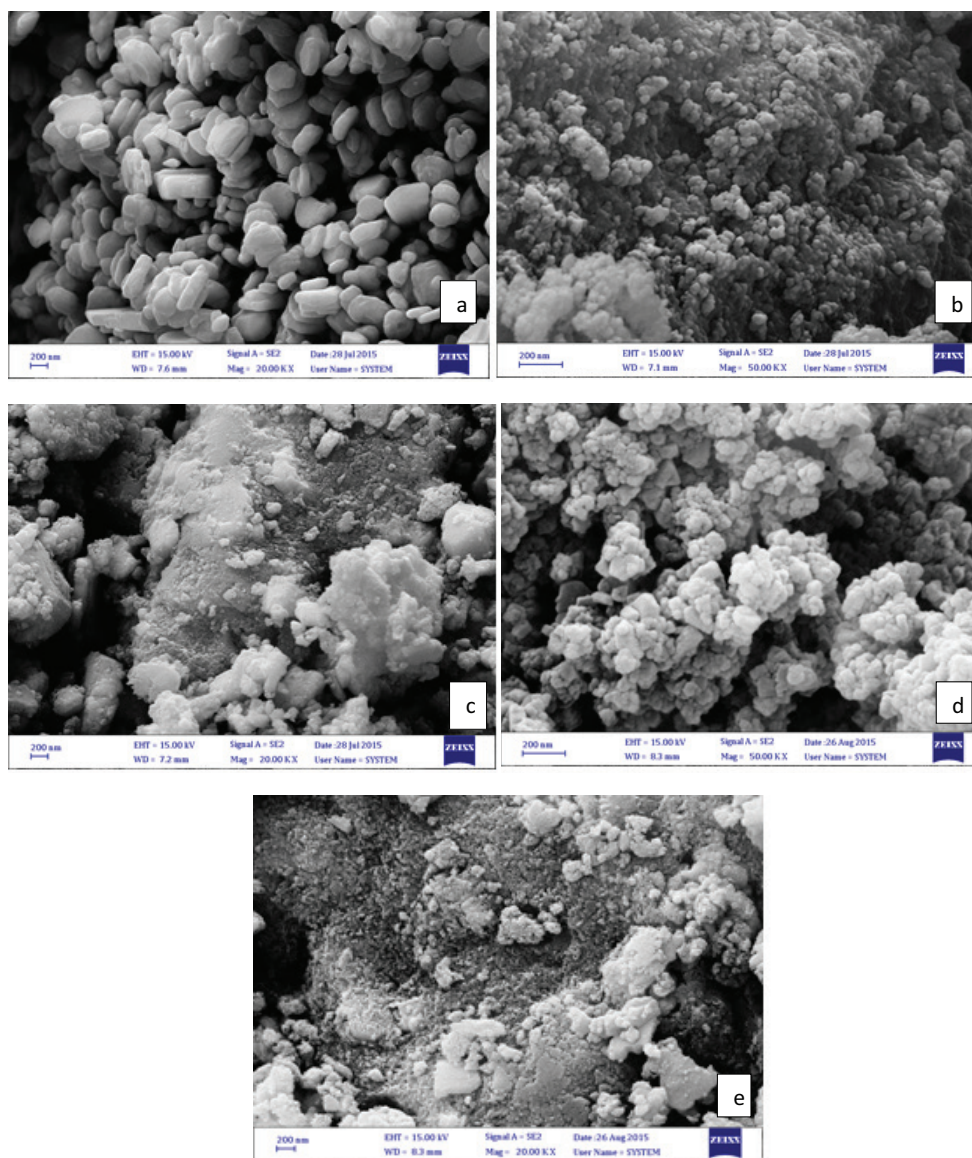
Fig. 2. FESEM images of (a) WO$_3$ NPs, (b) Al$_2$O$_3$ NPs [29] and WO$_3$–Al$_2$O$_3$ nanocomposites with different molar ratios: (c) (1:1), (d) (1:2), (e) (2:1).

nanograin clusters was found in the sample that are not distributed uniformly. The presence of the cluster may be due to the large specific surface area of the NPs [34]. The FESEM image shows that the WO$_3$–Al$_2$O$_3$ nanocomposites consist of uniform WO$_3$ particles that were dispersed on the surface of alumina (Figs. 2(c)–(e)). Figs. 3(a)–(e) show the EDS spectra of the samples. The EDS spectrum presented in Fig. 3(a) consists of the elements W and O, while Fig. 3(b) shows the EDS spectra of Al$_2$O$_3$ NPs indicating that it is consisted of two elements (Al and O) [29]. The peaks corresponding in energy to the Al, W and O are clearly observed at their normal, indicating that the products contained these elements (Figs. 3(c)–(e)). The EDS spectra of the samples are shown without any impurities. Results of EDS analysis of samples are given in Table 3. This analysis showed that WO$_3$–Al$_2$O$_3$ nanocomposite (molar ratio 1:2) has uniform elemental distribution compared with the other two nanocomposites.

3.3. XRD analysis

The crystalline phase of the samples was measured by XRD analysis. The XRD patterns of the samples synthesized using different molar ratio are shown in Fig. 4. As shown in Fig. 4(a), all the peaks can be indexed to a pure orthorhombic crystalline phase of WO$_3$ (JCPDS no. 20–1324) and (JCPDS no. 24–0747) [35]. The characteristic signals of WO$_3$ were found at 2θ = 23.07, 23.55, 24.30, 26.56, 28.27, 33.23, 34.11, 35.52, 41.46, 45.44, 47.20, 48.23, 49.87, 50.67, 53.63, 54.75, 55.77, 56.6, 58.31, 60.11, 62.12, 71.85 and 76.90 correspond to diffraction from the (002), (020), (200), (120), (112), (022), (202), (132), (004), (040), (400), (024), (042), (240), (402), (420), (034), (340), (414) and (422) in this figure. It can be seen that the XRD data for the Al$_2$O$_3$ NPs [29] match well with the standard card (JCPDS no. 10–0425). The peaks around 2θ = 37.01°, 39.43°, 45.85°, 60.8° and 66.75° are corresponds to the diffraction of the (311),

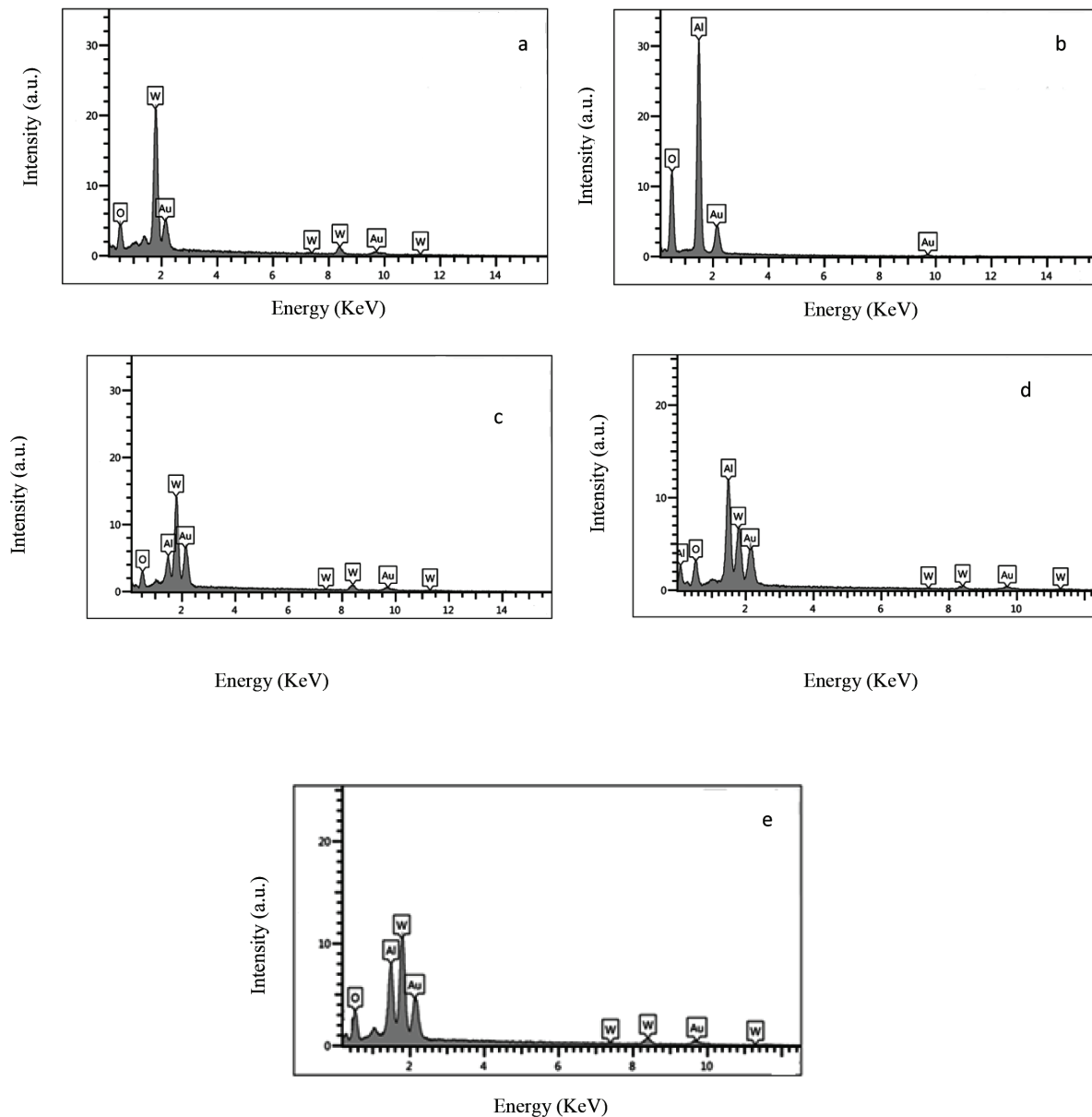Fig. 3. EDS spectra of (a) WO$_3$ NPs, (b) Al$_2$O$_3$ NPs [29] and WO$_3$–Al$_2$O$_3$ nanocomposites with different molar ratios: (c) (1:1), (d) (1:2), (e) (2:1).

Table 3
The EDS analysis of samples

Elements/wt%	WO$_3$	Al$_2$O$_3$	WO$_3$–Al$_2$O$_3$ (1:1)	WO$_3$–Al$_2$O$_3$ (1:2)	WO$_3$–Al$_2$O$_3$ (2:1)
O	12.7	39.5	11.2	26.5	23.2
Al	–	60.5	7.3	26.0	25.3
W	87.3	–	81.6	47.5	51.5
Total	100	100	100	100	100

(222), (400), (511) and (440) which confirms the presence a dual-phase system that consisting of cubic γ-Al$_2$O$_3$ and tetragonal γ-Al$_2$O$_3$ [36]. In Figs. 4(c)–(e), the XRD patterns show that nanocomposites have an optimal proportion of two-phase structure: WO$_3$ and Al$_2$O$_3$. The diffraction peaks observed at

2θ values of 35.49°, 45.58°, 60.09° and 67.05° are attributed to the γ-Al$_2$O$_3$ phase of nanocomposites structure and the other peaks are ascribed to the formation of WO$_3$ phase.

The average crystallite size of the samples was calculated by the Debye–Scherrer equation:

$$D = \frac{k\lambda}{\beta\cos\theta} \tag{2}$$

where D represents the average crystallite size, k is the shape factor ($k = 0.89$), λ denotes the wavelength of the X-ray radiation ($\lambda = 1.5406$ Å), β represents the full-width at half-maximum of the peak, and θ is the Bragg angle. The calculated average crystallite sizes are summarized in Table 4, which shows the average crystallite size of the samples ranges from 2 to 4.3 nm.

3.4. Surface area measurement

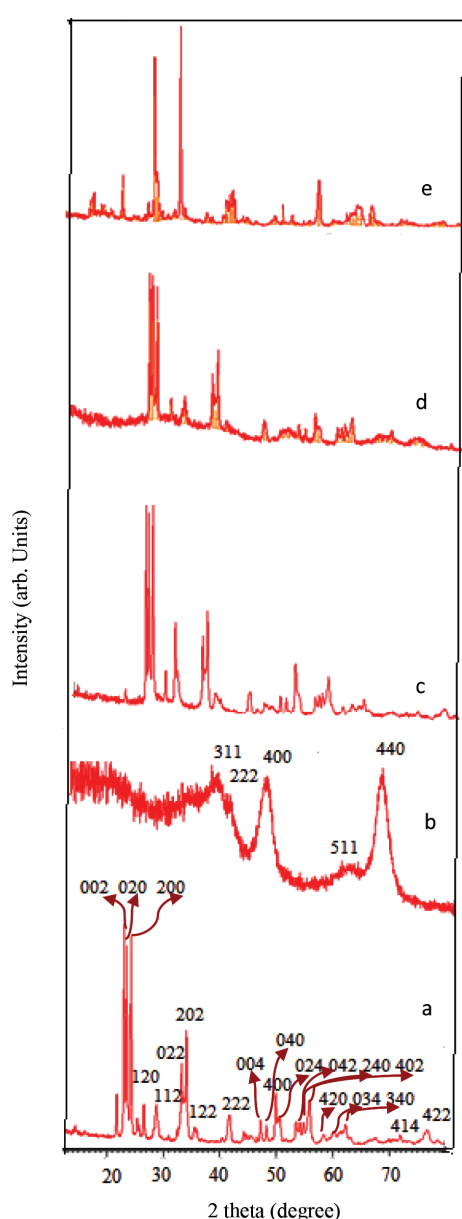The surface area of WO_3 NPs and WO_3–Al_2O_3 nanocomposites (molar ratio 1:1) were analyzed using BET method

and are listed in Table 5. These data show that specific surface area of WO_3–Al_2O_3 nanocomposite (molar ratio 1:1) was being significantly larger than those of WO_3 NPs. Furthermore, the pore volumes and pore size of samples were determined by using BJH method. Our data show that amesopore structures of the pores (Table 5). Moreover, the pore volume is slightly increased with incorporation of Al_2O_3 into WO_3 NPs.

3.5. PL properties

The photoluminescence (PL) is an efficient and sensitive tool for investigating the efficiency of charge transfer and electron–hole pairs separation from semiconductors [37]. The PL excitation spectra of samples are shown in Fig. 5. All the samples were evaluated in the emission range 400−100 nm. It can be seen two small peaks at 624 and 806 nm (Fig. 5(a)). The PL spectrum of the Al_2O_3 NPs displays two strong peaks at 434 and 760 nm (Fig. 5(b)). That is different from those of WO_3–Al_2O_3 nanocomposites but is similar to those of Al_2O_3 NPs (Figs. 5(c)–(e)). The reason for this phenomenon might be attributed to an efficient charge separation process by transformation of electrons of WO_3 to Al_2O_3, and the separation of electron–hole pairs that can cause enhancement of photocatalytic activity of WO_3–Al_2O_3 nanocomposites for degradation of CR.

3.6. Effect of molar ratio

The photocatalytic activity of pure WO_3 NPs and WO_3–Al_2O_3 nanocomposites (molar ratios 1:1, 1:2 and 2:1) in aqueous solution for degradation of CR was investigated under UV and visible light for 0, 15, 30, and 45 min of irradiation time (Fig. 6). The results show that incorporation of Al_2O_3 into WO_3 plays a powerful role in increasing the photocatalytic activity of WO_3–Al_2O_3 nanocomposite and the efficiency of photocatalytic activity for WO_3–Al_2O_3 with molar ratio (1:1) is higher than those molar ratios. Various factors can be attributed to the high photocatalytic activity observed

Fig. 4. XRD patterns of (a) WO_3 NPs, (b) Al_2O_3 NPs [29] and WO_3–Al_2O_3 nanocomposites with different molar ratios: (c) (1:1), (d) (1:2), (e) (2:1).

Table 4
The average crystallite size of the catalysts prepared at different molar ratios

Samples	Crystallite size (nm)
WO_3	4.3
Al_2O_3	2
WO_3–Al_2O_3 (1:1)	4.1
WO_3–Al_2O_3 (1:2)	3.3
WO_3–Al_2O_3 (2:1)	4

Table 5
Specific surface area values and pore parameters of WO_3 NPs and WO_3–Al_2O_3 nanocomposites (1:1)

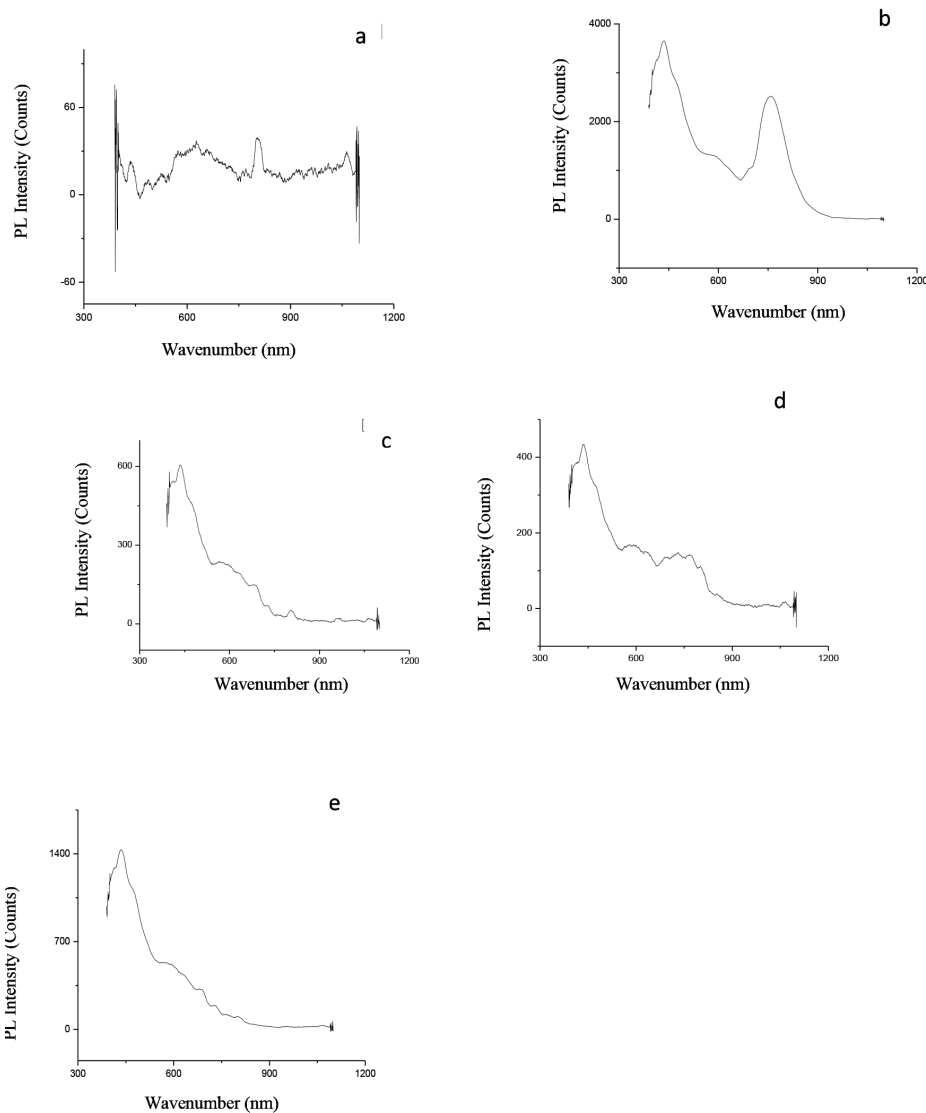| Samples	Surface area (m² g⁻¹)	Pore volume (cc g⁻¹)	Pore diameter (nm)
WO_3	2.8338	0.004	2.448
WO_3–Al_2O_3 (1:1)	41.8011	0.038	1.938

Fig. 5. Photoluminescence spectra of (a) WO₃ NPs, (b) Al₂O₃ NPs and WO₃–Al₂O₃ nanocomposites with different molar ratios: (c) (1:1), (d) (1:2), (e) (2:1).

in WO_3–Al_2O_3 (molar ratios 1:1). At first instance, a minor aggregation of the particles of WO_3–Al_2O_3 (molar ratios 1:1) with respect to other samples was observed (Fig. 2(c)). This promotes a better dispersion of the photocatalytic during the photocatalytic experiment. Regarding the surface area, WO_3–Al_2O_3 (molar ratios 1:1) has a higher exposed surface (Table 5). The photodegradation percentage of pure WO_3 NPs and WO_3–Al_2O_3 photocatalysts are given in Table 6. These data confirmed previous results in details, that is, by changing the ratio of Al_2O_3 in the composite, photodegradation percentage for molar ratio (1:1) is significantly higher than the other molar ratios [(1:2),(2:1)]. Furthermore, photodegradation under visible light is slightly higher than UV light. The photocatalytic activity should be enhanced by increasing the surface area and light absorption intensity and the decrease of electron–hole pair recombination in WO_3 with the incorporation of Al_2O_3 in the composite which can be emphasized by PL results.

Solution pH is an important parameter that affects photocatalytic processes because of different modification of surface properties. The pH effect on the photocatalytic degradation of CR (5 mg L⁻¹) was investigated at pH 3.5, 6.5, 9.5 and constant photocatalyst dosage (0.1 g) on WO_3–Al_2O_3 (molar ratio 1:1) as the best sample, under irradiation with UV and visible light (Fig. 7). Increasing and decreasing of pH was adjusted by adding HCl (0.1 mol L⁻¹) and NaOH (0.01 mol L⁻¹), respectively. The most degradation efficiency of CR was observed at pH 3.5 (95% and 100% degradation for UV and visible light, respectively).

The zero point charge (zpc) of WO_3–Al_2O_3 was determined to be 6 [38] and the surface is positively charged in acidic solution $pH < pH_{zpc}$ and negatively charged in alkaline solution $pH > pH_{zpc}$. The removal of CR as an anionic dye will increase with decreasing pH. Hence, lower pH (pH 3.5 in this study) caused significant enhancement on the photocatalytic degradation due to the increasing electrostatic attraction

between CR and surface of photocatalyst. Furthermore, because of presence of an excess hydroxyl group in acidic solution on the photocatalystic surface and formation of more hydroxyl radical [39], degradation of CR increased at pH 3.5 (Eq. (3)):

$$M - OH + H^+ \rightarrow M - OH - H^+ \rightarrow M - H_2O^+ \tag{3}$$

$$MO^+ + Dye^- \rightarrow M - O - Dye \tag{4}$$
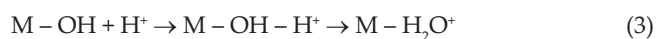
The effect of dosage on the photocatalytic degradation of CR was examined under the range of 0.025-0.1 g
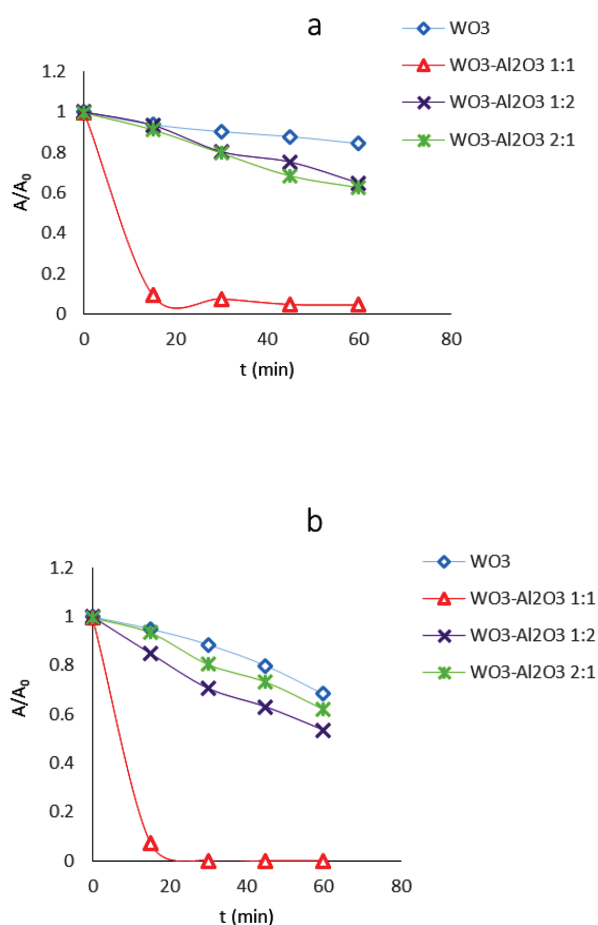

Fig. 6. Comparative photocatalytic degradation of CR with pure WO_3 NPs and WO_3–Al_2O_3 nanocomposites under UV (a) and visible (b) light.

for WO_3–Al_2O_3 (molar ratio 1:1), as the best sample constant CR concentration 5 mg L^{-1} and pH 3.5. As shown in Fig. 8, photocatalytic degradation of CR was increased with increasing photocatalyst dosage from 0.025 to 0.1 g. This increase may be explained by increasing the total active sites on the catalyst surface and consequently, number of adsorbed dye molecules will be increased. However, for very high photocatalyst dosage, the turbidity of the suspension will be increased, and it causes blockage of the incident light [39].

4. Photocatalytic mechanism

The mechanism of photocatalytic degradation of CR under the UV–Vis light for WO_3–Al_2O_3 nanocomposite is portrayed in Fig. 9. When the photocatalyst is irradiated by UV–Vis light irradiation, the electrons are excited from the valence band (VB) of WO_3 photocatalyst to the conduction band (CB) Al_2O_3 by creating the negative electron (e$^-$) and positive–hole (h$^+$) pair in the VB (Eq. (5)) [40]. The electron–hole pairs lead to the formation of OH$^\bullet$, O$_2^\bullet$ and HOO$^\bullet$ that
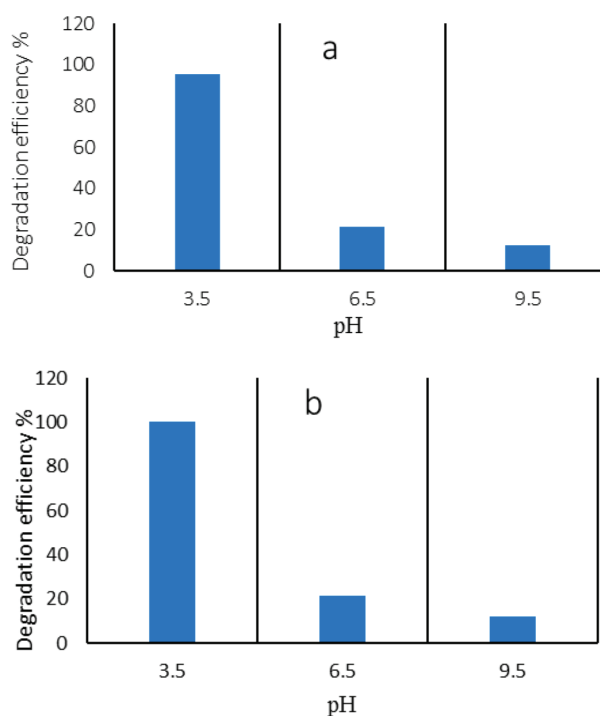

Fig. 7. Effect of pH on the photocatalytic degradation of CR under UV (a) and visible (b) light.

Table 6
Data of CR photocatalytic degradation in the presence of pure WO_3 NPs and WO_3–Al_2O_3 photocatalysts

Samples	Irradiation time for visible (min)	Irradiation time for UV (min)	Photodegradation ratios for visible (%)	Photodegradation ratios for UV (%)
WO_3	45	45	20	12.16
WO_3–Al_2O_3 (1:1)	30	45	100	95
WO_3–Al_2O_3 (1:2)	45	45	36.89	24.73
WO_3–Al_2O_3 (2:1)	45	45	37.96	31.68

Fig. 9. Photocatalytic mechanism schematic of the WO_3–Al_2O_3 nanocomposites.
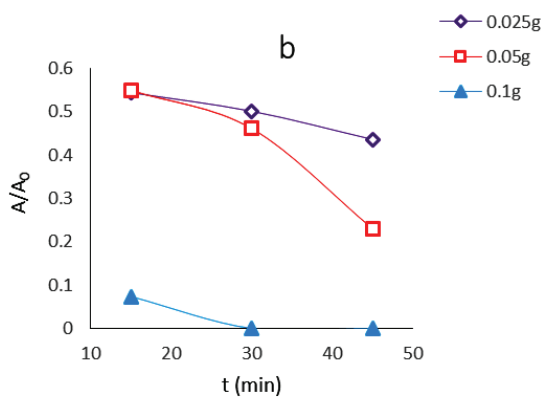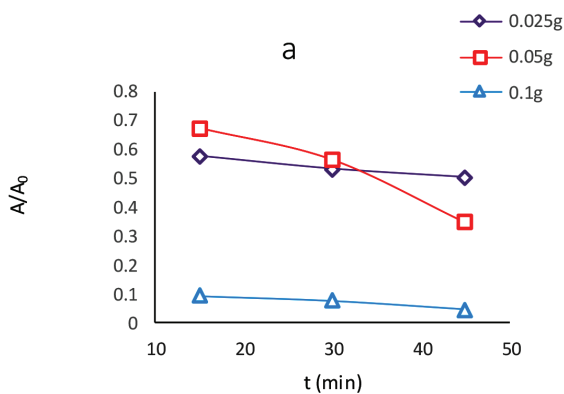
Fig. 8. Effect of photocatalyst dosage on the photocatalytic degradation of CR under UV (a) and visible (b) light.

are oxidizing species in the photocatalytic oxidation processes [40].

$$WO_3 - Al_2O_3 \rightarrow Al_2O_3 (e^-) + WO_3 (h^+) \tag{5}$$

The hydroxyl radical production is formed as follows:

$$h^+ + H_2O \rightarrow OH^\bullet + H^+ \tag{6}$$

$$h^+ + OH^- \rightarrow OH^\bullet \tag{7}$$

Furthermore, excited electrons into the CB (e^-) on the surface of photocatalyst can reduce O_2 to susperoxide anion $OH^\bullet$ radical that generated as Eqs. (6) and (7) acts as an oxidation factor for mineralization of CR as follows [40]:

$$Dye + OH^\bullet \rightarrow CO_2 + H_2O \tag{8}$$

$$Dye + h^+ \rightarrow CO_2 + H_2O \tag{9}$$
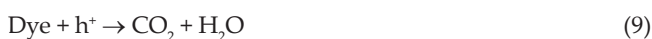
Moreover, h^+ can act as an oxidation factor. These processes effectively suppress the electron–hole recombination and produce excess $OH^\bullet$ radicals necessary for degradation of CR. The presence of surface-generated reactive species such as $OH^\bul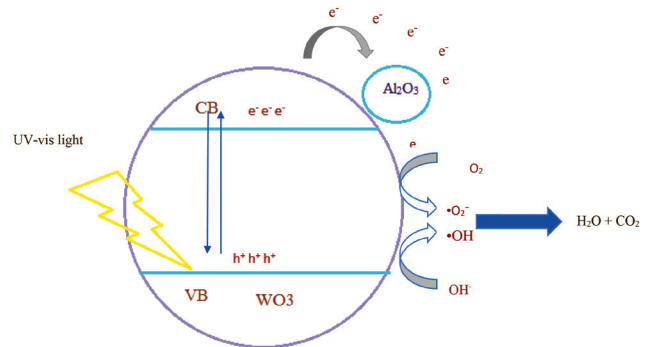let$ and $O_2^\bullet$ on the photocatalysts was employed to investigate the photocatalytic mechanism of WO_3–Al_2O_3 nanocomposite under UV and visible light. The results indicated that $OH^\bullet$ could be produced on the VB under both UV and visible light irradiation, but more $OH^\bullet$ species were generated under visible irradiation. The incorporation of Al_2O_3 into WO_3 played an important role in the enhancement of photocatalytic activity.

A large number of photocatalysts used for the degradation of CR but there has not been any research about the use of WO_3–Al_2O_3 nanocomposite as photocatalytic degradation of CR under UV and visible light. Therefore, this study compared the photocatalytic degradation of CR with that of other literature. This comparison is summarized in Table 7. Lam et al. [41] have reported 95.12% of degradation of CR within 120 min. Guy et al. [21] have reported 98.2% of degradation of CR within 60 min. The degradation percentage of CR was achieved 95% and 100%, under UV and visible light, respectively (Fig. 6). As can be seen in Table 7, the WO_3–Al_2O_3 photocatalyst has the highest photocatalytic degradation. The WO_3–Al_2O_3 photocatalyst obtains a short-period degradation of CR under UV and visible light.

5. Conclusions

In this study, the effects of WO_3:Al_2O_3 ratios on the photocatalytic properties of WO_3–Al_2O_3 nanocomposites which are synthesized by sol-gel method were investigated. The nanocomposites were characterized by FTIR, XRD, FESEM, EDS, PL, BET and BJH. Specific surface area and photocatalytic properties of WO_3 improved by the formation WO_3–Al_2O_3 nanocomposite. The photocatalytic activity of as-prepared photocatalysts was examined by the degradation of CR under UV and visible light irradiation. It was revealed that photocatalytic activity of WO_3 NPs is markedly lower than those WO_3–Al_2O_3 nanocomposites. The best photocatalytic activity was obtained with WO_3–Al_2O_3 nanocomposite at molar ratio 1:1 for UV and visible light. The reason behind its higher activity was associated with factors such as morphology, aggregation degree of its particles and surface area. The optimized reaction conditions are pH 3.5, photocatalyst dosage 0.1 g and initial CR concentration 5 mg L^{-1} under UV and visible irradiation. Finally, the results of this study reveal that WO_3–Al_2O_3 nanocomposite is suitable for the degradation of CR.

Table 7
Comparison of photocatalytic degradation of CR

S. No.	Catalyst	Light source	Time (min)	Degradation (%)	References
1	Pd/ZnO	100 W-UV lamp	60	98.2	[21]
2	SrFeO$_{19}$	125 W-Hg lamp	180	90	[40]
3	WO$_3$–TiO$_2$/AC	500 W-Hg lamp	120	95.12	[41]
4	CuO	18 W-UV lamp	210	67	[42]
5	ZnO–CdS	250 W-Hg lamp	100	88	[43]

Acknowledgment

References

[1] A. Nezamzadeh-Ejhieh, N. Moazzeni, Sunlight photodecolorization of a mixture of methyl orange and bromocresol green by CuS incorporated in a clinoptilolite zeolite as a heterogeneous catalyst, J. Ind. Eng. Chem., 19 (2013) 1433–1442.

[2] M. Safari, M. Nikazar, M. Dadvar, Photocatalytic degradation of methyl tert-butyl ether (MTBE) by Fe-TiO$_2$ nanoparticles, J. Ind. Eng. Chem., 19 (2013) 1697–1702.

[3] A. Capra, B. Scicolone, Emitter and filter tests for wastewater reuse by drip irrigation, Agric. Water Manage., 68 (2004) 135–149.

[4] N. Mathur, P. Bhatnagar, P. Bakre, Assessing mutagenicity of textile dyes from Pali(Rajasthan) using Ames bioassay, Appl. Ecol. Environ. Res., 4 (2005) 111–118.

[5] C. Namasivayam, D. Kavitha, Removal of Congo Red from water by adsorption onto activated carbon prepared from coir pith, an agricultural solid waste, Dyes Pigments., 54 (2002) 47–58.

[6] M.K. Purkait, A. Maiti, S. Das Gupta, S. De, Removal of Congo red using activated carbon and its regeneration, J. Hazard. Mater., 145 (2007) 287–295.

[7] G. Crini, Non-conventional low-cost adsorbents for dye removal: a review, Bioresour. Technol., 97 (2006) 1061–1085.

[8] M. Khadhraoui, H. Trabelsi, M. Ksibi, S. Bouguerra B. Elleuch, Discoloration and detoxicification of a Congo red dye solution by means of ozone treatment for a possible water reuse, J. Hazard. Mater., 161 (2009) 974–981.

[9] G.K. Parshettia, A.A. Telkeb, D.C. Kalyanib, S.P. Govindwarb, Decolorization and detoxification of sulfonated azo dye methyl orange by *Kocuria rosea* MTCC 1532, J. Hazard. Mater., 176 (2010) 503–509.

[10] R. Andreozzi, V. Caprio, A. Insola, R. Marotta, Advanced oxidation processes (AOP) for water purification and recovery, Catal. Today, 53 (1999) 51–59.

[11] G. Busca, S. Berardinelli, C. Resini, L. Arrighi, Technologies for the removal of phenol from fluid streams: a short review of recent developments, J. Hazard. Mater., 160 (2008) 265–288.

[12] J.M. Herrmann, Heterogeneous photocatalysis: fundamentals and applications to the removal of various types of aqueous pollutants, Catal. Today., 53 (1999) 115–129.

[13] T.Y. Ma, Z.Y. Yuan, J.L. Cao, Hydrangea-like meso-/macroporous ZnO-CeO$_2$ binary oxide materials: synthesis, photocatalysis and CO oxidation, Eur. J. Inorg. Chem., 5 (2010) 716–724.

[14] X.H. Zhang, X.H. Lu, Y.Q. Shen, J.B. Han, L.Y. Yuan, L. Gong, Z. Xu, X.D. Bai, M. Wei, Y.X. Tong, Y.H. Gao, J. Chen, J. Zhou, Z.L. Wang, Three-dimensional WO$_3$ nanostructures on carbon paper: photoelectrochemical property and visible light driven photocatalysis, Chem. Commun., 47 (2011) 5804–5806.

[15] K. Maeda, M. Higashi, D.L. Lu, R. Abe, K. Domen, Efficient nonsacrificial water splitting through two-step photoexcitation by visible light using a modified oxynitride as a hydrogen evolution photocatalyst, J. Am. Chem. Soc., 132 (2010) 5858–5868.

[16] Y. Wang, Y. Su, L. Qiao, L. Liu, Q. Su, C. Zhu, X. Liu, Synthesis of one-dimensional TiO$_2$/V$_2$O$_5$ branched heterostructures and their visible light photocatalytic activity towards rhodamine B, Nanotechnology, 22 (2011) 225702.

[17] R. Georgekutty, M.K. Seenry, S.C. Pillai, A highly efficient Ag-ZnO photocatalyst: synthesis, properties, and mechanism, J. Phys. Chem. C., 112 (2008) 13563–13570.

[18] Y. Zheng, C. Chen, Y. Zhan, X. Lin, Q. Zheng, K. Wei, J. Zhu, Photocatalytic activity of Ag/ZnO heterostructure nanocatalyst: correlation between structure and property, J. Phys. Chem. C., 112 (2008) 10773–10777.

[19] J.B. Zhong, J.Z. Li, X.Y. He, J. Zeng, Y. Lu, W. Hu and K. Lin, Improved photocatalytic performance of Pd-doped ZnO, Curr. Appl. Phys., 12 (2012) 998–1001.

[20] J. Miao, A. Xie, S. Li, F. Huang, J. Cao, Y. Shen, A novel reducing graphene/polyaniline/cuprous oxide composite hydrogel with unexpected photocatalytic activity for the degradation of Congo red, Appl. Surf. Sci., 360 (2016) 594–600.

[21] N. Guy, S. Cakar, M. Ozacar, Comparison of palladium/zinc oxide photocatalysts prepared by different palladium doping methods for Congo red degradation, J. Colloid Interf. Sci., 466 (2016) 128–137.

[22] S. Shukla, S. Chaudhary, A. Umar, G.R. Chaudhary, S.K. Mehta, Surfactant functionalized tungsten oxide nanoparticles with enhanced photocatalytic activity, Chem. Eng. J., 288 (2016) 423–431.

[23] H. Xiao, F. Qu, A. Umar, X. Wu, Facile synthesis of SnO$_2$ hollow microspheres composed of nanoparticles and their remarkable photocatalytic performance, Mater. Res. Bull., 74 (2016) 284–290.

[24] A. Mayoufi, M. Faouzi Nsib, O. Ahmed, A. Houas, Synthesis, characterization and photocatalytic performance of W, N, S-tri-doped TiO$_2$ under visible light irradiation, C. R. Chimie., 18 (2015) 875–882.

[25] E.S. Aazam, Photocatalytic degradation of Congo red under visible light irradiation using Pd–Bi$_{3.84}$W$_{0.16}$O$_{6.24}$ nanocomposite, J. Alloys Compd., 644 (2015) 1–6.

[26] D. Ljubas, G. Smoljanic, H. Juretic, Degradation of methyl orange and Congo red dyes by using TiO$_2$ nanoparticles activated by the solar and the solar-like radiation, J. Environ. Manage., 161 (2015) 83–91.

[27] D. Sanchez Martinez, A. Martinez-dela Cruz, E. Lopez Cuellar, Photocatalytic properties of WO$_3$ nanoparticles obtained by precipitation in presence of urea as complexing agent, Appl. Catal., A, 398 (2011) 179–186.

[28] A. Amirsalari, S. Farjami Shayesteh, Effects of pH and calcination temperature on structural and optical properties of alumina nanoparticles, Superlattices Microstruct., 82 (2015) 507–524.

[29] M. Firouzi, A. Nouri, Synthesis, characterization and application of alumina nanoparticles for photocatalytic degradation of Congo red dye, J. Appl. Chem., 12 (2017) 23–34.

[30] M.F. Daniel, B. Desbat, J.C. Lassegues, B. Gerand, M. Figlarz, Infrared and Raman study of WO$_3$ tungsten trioxides and WO$_3$, xH$_2$O tungsten trioxide tydrates, J. Solid State Chem., 67 (1987) 235–247.

[31] Z. Guo, T. Pereira, O. Choi, Y. Wang, H.T. Hahn, Surface functionalized alumina nanoparticle filled polymeric nanocomposites with enhanced mechanical properties, Mater. Chem., 16 (2006) 2800–2808.

[32] W. Lv, Q. Qiu, F. Wang, S. Wei, B. Liu, Z. Luo, Sonochemical synthesis of cobalt aluminate nanoparticles under various preparation parameters, Ultrason. Sonochem., 17 (2010) 793–801.

[33] U. Janosovits, G. Ziegler, U. Scharf, A. Wokaun, Structural characterization of intermediate species during synthesis of Al_2O_3 – aerogels, J. Non-Cryst. Solids, 210 (1997) 1–13.

[34] S. Farhadi, S. Panahandehjoo, Spinel-type zinc aluminate $(ZnAl_2O_4)$ nanoparticles prepared by the co-precipitation method: a novel, green and recyclable heterogeneous catalyst for the acetylation of amines, alcohols and phenols under solvent-free conditions, Appl. Catal., A, 382 (2010) 293–302.

[35] R. Abazari, A.R. Mahjoub, L.A. Saghatforoush, S. Sanati, Characterization and optical properties of spherical WO_3 nanoparticles synthesized via the reverse microemulsion process and their photocatalytic behavior, Mater. Lett., 133 (2014) 208–211.

[36] Y. Liu, D. Ma, X. Han, X. Bao, W. Frandsen, D. Wang, D. Su, Hydrothermal synthesis of microscale boehmite and gamma nanoleaves alumina, Mater. Lett., 62 (2008) 1297–1301.

[37] Z. Jin, W. Duan, W. Duan, B. Liu, X. Chen, F. Yang, J. Guo, Indium doped and carbon modified P25 nanocomposites with high visible-light sensitivity for the photocatalytic degradation of organic dyes, Appl. Catal., A, 517 (2016) 129–140.

[38] F.J. Gil Llambías, J. Salvatierra, L. Bouyssieres, M. Escudey, Hydrodesulfurization activity of WO_3/γ-alumina prepared by the equilibrium adsorption method, Appl. Catal., 59 (1990) 185–195.

[39] K. Vignesh, M. Rajarajan, A. Suganthi, Visible light assisted photocatalytic performance of Ni and Th co-doped ZnO nanoparticles for the degradation of methylene blue dye, J. Indust. Eng. Chem., 20 (2014) 3826–3833.

[40] O. Mohanta, Y.N. Singhbabu, S.K. Girri, D. Dadhich, N.N. Das, R.K. Sahu, Degradation of Congo red pollutants using microwave derived $SrFe_{12}O_{19}$: an efficient magnetic photocatalyst under visible light, J. Alloys Compd., 564 (2013) 78–83.

[41] S.M. Lam, J.C. Sin, A.Z. Abdullah, A.R. Mohamed, Transition metal oxide loaded ZnO nanorods: preparation, characterization and their UV–Vis photocatalytic activities, Sep. Purif. Technol., 132 (2014) 378–387.

[42] R. Lamba, A. Umar, S.K. Mehta, S.K. Kansal, Well-crystalline porous ZnO–SnO 2 nanosheets: an effective visible-light driven photocatalyst and highly sensitive smart sensor material, Talanta, 131 (2015) 490–498.

[43] W. Zhao, Y. Guo, Y. Faiz, W.T. Yuan, C. Sun, S.M. Wang, Y.H. Deng, Y. Zhuang, Y. Li, X.M. Wang, H. He, S.G. Yang, Facile in-suit synthesis of $Ag/AgVO_3$ one-dimensional hybrid nanoribbons with enhanced performance of plasmonic visible-light photocatalysis, Appl. Catal., B, 163 (2015) 288–297.